

A flexure-based electromagnetic nanopositioning actuator with predictable and re-configurable open-loop positioning resolution

Tat Joo Teo^{a,*}, Guilin Yang^b, I-Ming Chen^c

^a Mechatronics Group, Singapore Institute of Manufacturing Technology, Singapore 638075, Singapore

^b Ningbo Institute of Materials Technology and Engineering, Chinese Academy of Sciences, Zhejiang Province 315201, China

^c School of Mechanical and Aerospace Engineering, Nanyang Technological University, Singapore 639798, Singapore

A B S T R A C T

This paper presents a novel cylindrical-shaped Flexure-based Electromagnetic Linear Actuator (FELA) that exhibits predictable and re-configurable open-loop positioning resolution. By combining contactless Lorentz-force actuation and frictionless flexure-based supporting bearings, it produces high repeatable motion and sub-micron positioning resolution. In this paper, the design concept of this cylindrical-shaped FELA will be introduced. It focuses on the modeling of the flexure-based supporting bearings, the thermal modeling of the electromagnetic module, and the unique characteristics of FELA, i.e., predictable and re-configurable open-loop positioning resolution. A prototype was developed to evaluate the performance and demonstrate these unique characteristics of this new class of nanopositioning actuator.

Keywords:

Flexure joints
Semi-analytic model
Lorentz-force actuation
Nanopositioning actuator
Thermal modeling
Lumped capacitance model
Flexure modeling

1. Introduction

An actuator with nano-positioning capabilities has been the key technology in nano-/micro-scale manufacturing processes such as nano-imprint lithography, fibre optics alignment, MEMS assembly, nano-scale machining, etc. Among various types of nano-positioning actuators, the solid-state piezoelectric (PZT) actuators have been the most popular choice due to their large actuating force and high stiffness. However, PZT actuators have limited displacements that make them unsuitable to drive high-precision manipulators targeted for large traveling range [1]. Although some existing high-precision positioning actuators are able to eliminate such limitations, the displacement amplification techniques that are used within these actuators inherit other drawbacks. For example, PZT-driven actuators that use high-pitch screw actuating-shaft to achieve millimeters of displacement have poor repeatability due to backlash and Coulomb friction [2]. Others that use the magnetostrictive clamping technique [3], the inchworm clamping [4], and the impact-force method [5] to drive an internal shaft for

displacement amplification purposes have low payload capacities. In addition, the slow response speed makes these actuators inefficient for high speed applications.

Electromagnetic driving scheme has the potential of delivering millimeters of traveling range with nanometers of positioning resolution. Actuators of such frictionless drive, i.e., voice-coil linear actuators and solenoid actuators, have also been employed in high-precision manipulation [6,7]. However, the voice-coil actuator produces relatively small output forces (or poor force sensitivity). Although the moving magnet actuator offers good dynamic behavior and good heat dissipation, the magnetic force attraction due to the external iron casing causes the output force to be inconstant throughout the entire displacement stroke [8]. A solenoid actuator offers good force sensitivity but is unable to achieve a constant output force throughout its allowable traveling range due to the nonlinearity between force and displacement [9]. Furthermore, magnetization on the ferromagnetic stator introduces nonlinear magnetic hysteresis that leads to inaccuracy in nanometric positioning tracking [10]. The drawbacks of existing nano-positioning actuators motivated the development of a Flexure-based Electromagnetic Linear Actuator (FELA) [11]. FELA is formed through a marriage between an electromagnetic (EM) driving scheme and the flexure joints to achieve a few millimeters of displacement, large continuous thrust force, and a direct-force control capability. From past literatures [12,11], FELA was able to deliver a positioning

* Corresponding author at: Mechatronics Group, Singapore Institute of Manufacturing Technology, 71 Nanyang Drive, Singapore 638075, Singapore.
Tel.: +65 67938285.

E-mail address: tjteo@SIMTech.a-star.edu.sg (T.J. Teo).

accuracy of ± 20 nm, a continuous output force of 60 N/A, an actuating speed of more than 100 mm/s throughout a large displacement stroke of 4 mm.

In our previous research efforts, the thermal management of FELA was not considered because its applications were mainly on automating embossing [13,14] and nano-imprinting processes [15,16] to replicate micro/nano-scale features. In these processes, large output force with direct precise force feedback is essential. Hence, high force generation and high motion repeatability were the key considerations during the design phase. In addition, the closed-loop feedback control implemented on the end-effector ensures any form of thermal expansion will not affect the positioning accuracy. Thus, the coils usually operate between 60 and 80 °C during those imprinting operations. However, recent challenges arisen from applications such as the optical fiber alignment and the bio-cell manipulation have demanded FELA to produce higher positioning and thermal stability over a few minutes of operation period with or without closed-loop feedback control. Thus, an improved version, which could meet such requirements, is required for those applications. In our recent research efforts, a model-based thermal compensation control was implemented to the existing FELA to compensate for the material expansion at the tip of the output shaft due to thermal induction from the energized coil [17]. This investigation shows that the effectiveness of thermal control largely depends on the amount of thermocouple sensors used to estimate the thermally induced position error. To reduce the complexity of the entire control system, a two-stage optimization method was explored to re-design the Electromagnetic (EM) module of the existing FELA [18]. These efforts led to the conclusion that by factoring the thermal effect in the initial design stage will be much effective over the thermal control or thermal management approach in the later stages.

This paper presents a novel cylindrical-shaped FELA that achieves lower heat generation as compared to the existing rectangular-shaped FELA. It consists of a new Lorentz-force Electromagnetic (EM) module and flexure-based membrane supporting bearings. In this work, the cylindrical-shaped FELA has targeted specifications of ± 10 nm positioning accuracy and ± 0.15 °C thermal stability over a stroke length of 2 mm at the end-effector. To achieve the desired thermal characteristic, an accurate thermal modeling of the EM module will be presented. To synthesize the desired stiffness characteristic that facilitate the EM module in achieving the targeted thermal stability, the stiffness modeling of the flexure-based membrane bearings was conducted using a novel semi-analytic modeling approach [19] and will also be presented in this paper. Most importantly, this paper also presents a unique characteristic of the FELA, i.e., predictable and re-configurable open-loop positioning resolution. Such characteristic cannot be found in existing nanopositioning actuators. All theoretical modeling and the unique characteristics of FELA will be evaluated and demonstrated.

2. Design concept of the novel cylindrical-shaped FELA

The cylindrical-shape FELA comprises of a new Lorentz-force EM module and a pair of flexure-based membrane support bearings as shown in Fig. 1. Termed as an Electromagnetic Driving Module (EDM), the Lorentz-force EM module is formed by a PM-based magnetic circuit with the moving air-core coil while the flexure-based membrane bearings are used to support both ends of the moving air-core coil in order to retain the contactless nature of the EM driving scheme. Consequently, the frictionless characteristic of both driving and supporting elements ensure high motion repeatability.

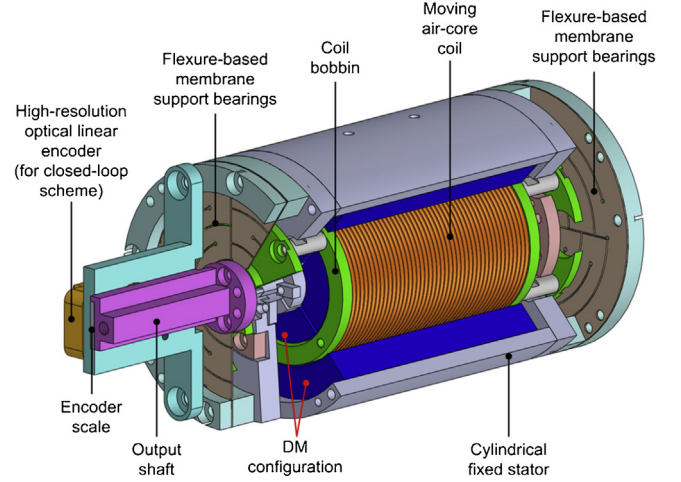


Fig. 1. A detailed breakdown on the cylindrical-shaped FELA.

2.1. A segmented dual-magnet configuration

In the previous EDM design [11], 50% of the moving air-core coil does not operate within the magnetic field regions. Assuming that this portion of coil could operate within the magnetic field regions, the overall force generation could be enhanced by up to 50% with the same amount of input current. In other words, only 50% of the input current would be needed to generate the equivalent amount of force that the previous EDM design is producing. Consequently, heat generation could be reduced by half. In this paper, a segmented Dual-Magnet (DM) configuration was proposed to ensure that the entire air-core coil is operating within the magnetic field regions as shown in Fig. 2a. Instead of a complete stator casing, the new cylindrical-shaped EDM was constructed by a group of segments whereby each segment was formed via a DM configuration as shown in Fig. 2b.

Based on a segmented architecture, the magnetic field travels from outer PM to the inner PM within the designated closed-loop ferrous path to reduce magnetic leakages. (Note: the magnetization direction of the outer and inner PMs are similar.) Thus, most of the magnetic field could be extracted from both PMs to enhance the magnetic flux density within the effective air gap, in which the moving air-core coil operates. The segmented concept also prevents demagnetization between two inner PMs or two outer PMs when packed closely together because of the designated closed-loop ferrous path from each segment. Such a concept also reduces the assembly time significantly since the PMs can be glued in each segment concurrently before assembling all the segments together. Lastly, the cylindrical DM configuration forms an encasement for the magnetic field and prevents magnetic field leakage to the environment. Hence, FELA can be used in certain applications and environment that are sensitive to EM or magnetic field disturbance.

Unlike conventional magnetic circuits [20,21] that deliver inconsistent and non-uniform magnetic flux density within the effective air gaps, the DM configuration delivers constant and evenly distributed magnetic flux density within a large effective air gap [22], i.e., 10 mm gap between the outer and inner PMs. By restricting the moving air-core coil to operate within the effective air gap as shown in Fig. 3, the new cylindrical-shaped EDM produces a constant current-force sensitivity (N/A) throughout the entire traveling range of the moving coil. Governed by the Lorentz-force principle and assuming that the magnetic flux density, B_{ext} , is perpendicular to the direction of input current, i , the output force, F , is expressed as

$$F \equiv iLB_{ext} \quad (1)$$

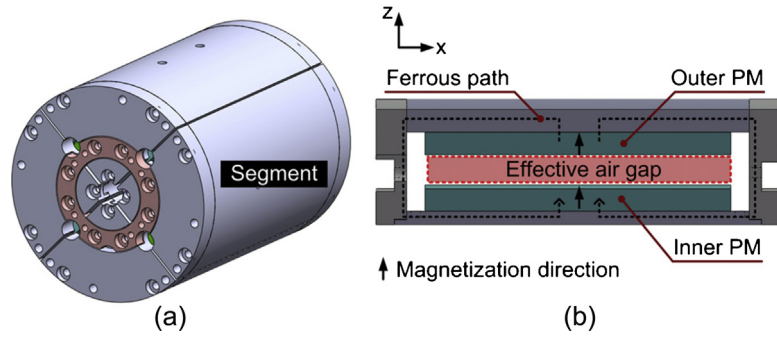


Fig. 2. (a) A cylindrical-shaped EDM constructed by a group of segmented DM configuration (US patent appl. #2013/990,219).

where L represents the total coil length operating within the effective air gap. Aided by the segmented DM configuration, Eq. (1) also suggest that the new cylindrical-shaped EDM provides a linear current–force relationship due to the constant magnetic flux density within the effective air gap. The modeling and optimization of the DM configuration have been presented in recent literatures [18,22]. This paper mainly focuses on the thermal modeling of the EDM.

2.2. Flexure-based membrane support bearings

To retain the contactless nature of the Lorentz-force EM driving scheme, flexure joints are used to develop frictionless bearings to support the moving air-core coil as illustrated in Fig. 3. Unlike other frictionless bearings such as the air bearings, the magnetic bearings, and the hydrostatic/hydrodynamic bearings, these flexure-based bearings do not require any air/electrical/fluid source, expensive sensors, nor complex control systems to function. As a result, flexure-based bearings are simple, inexpensive and maintenance-free. In addition, a well-designed flexure-based bearing ensures low stiffness in the actuating direction while providing relatively higher stiffness in all non-actuating directions within the allowable travel range. Unlike the previous FELA design, which used clamping blocks and stainless steel shims to form such flexure-based bearings [11], the new cylindrical-shaped FELA adopts a flexure-based membrane architecture that is formed by a single monolithic-cut stainless steel sheet. Consequently, the absence of the clamping blocks also eliminates these secondary moving masses. As the flexure-based bearings only operate within the elastic region of the material, the relationship between the force generated from the EDM and the output displacement, δ , of the air-core coil translator is assumed to be linear and expressed as

$$K = \frac{F}{\delta} \quad (2)$$

where K represents the stiffness of the flexure-based bearings.

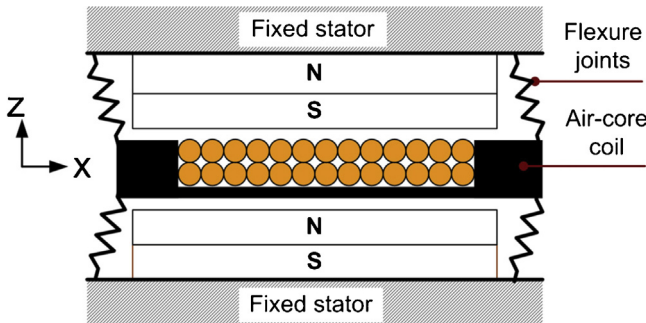


Fig. 3. Working principle of FELA: flexure-based bearings supporting a moving air-core coil that operates within the effective air gap of a DM configuration.

2.3. Re-configurable open-loop positioning resolution

Due to the linear current–force relationship of the EDM and the linear force–displacement relationship of the flexure-based bearings, the open-loop positioning resolution of FELA becomes predictable and re-configurable. (Note: an open-loop positioning resolution is defined as the achievable resolution based on the smallest controllable input current.) By combining the Ohm's Law, i.e., $V = IR$, with Eqs. (1) and (2), the open-loop positioning resolution of FELA is given as

$$\delta = \frac{V(R_{coil} + R_{ext})^{-1}LB_{ext}}{K} \quad (3)$$

where R_{coil} represents the resistance of the air-core coil and R_{ext} represents the resistance of the external resistor. Eq. (3) suggests two different approaches to enhance the open-loop positioning resolution of FELA. First, by increasing the stiffness of flexure-based bearings to enhance the positioning resolution for the same amount of driving force. Second, by adding external resistors between the voltage supply and the system to reduce the amount of current via the voltage mode. Flexibility to reconfigure the open-loop positioning resolution is a unique characteristic of FELA and will be demonstrated in later part of this paper.

3. Thermal modeling of the cylindrical-shaped EDM

Thermal modeling and analysis plays a crucial role in synthesizing the cylindrical-shaped EDM to achieve a desired power consumption and temperature characteristic for continuous force generation. In this work, the lumped capacitance modeling approach was used to obtain the mathematical representation of the thermal performance of the EDM.

3.1. Power management

From Eq. (1), the output force is a function of input current, magnetic flux density and the total coil length operating within the air gap. Based on the architecture of the cylindrical-shaped EDM, the coils are wound on a circular bobbin to form the moving air-core coil as shown in Fig. 4. Assuming that the coiling is ideal, the total number of rows will represent the total number of layers while each column will represent the number of turns per layer. Based on this configuration, the total coil length is represented as

$$L = 2\pi N_{tpl} [r_b N_l + OD(N_l + 1)(N_l/2)] \quad (4)$$

where N_l represents the number of layers of coil within a bobbin, N_{tpl} represents the number of turns per layer, OD represents the overall diameter of the conducting coil wire (with insulation

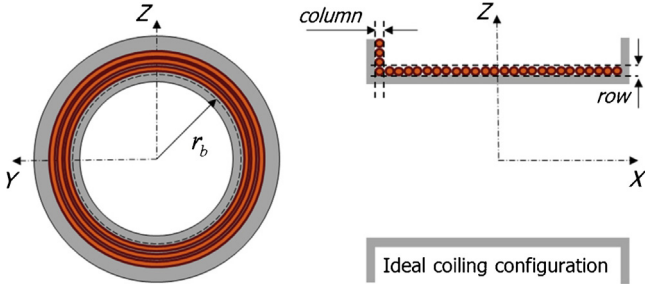


Fig. 4. A circular bobbin that holds the moving air-core coil.

layer), and r_b represents the radius of the bobbin. Subsequently, the internal coil resistance of the total coil length is given as

$$R_{coil} = \frac{\chi L}{\pi(ID/2)^2} \quad (5)$$

where χ represents the resistivity of the conducting material, i.e., $1.7 \times 10^{-8} \Omega m$ for copper wire, and ID represents the internal diameter or the core diameter of the conducting wire (excluding the insulation layer). With R_{coil} and input current, the power, Q , consumed by the EDM is expressed as

$$Q = i^2 R_{coil} \quad (6)$$

3.2. Lumped capacitance modeling approach

In nanopositioning applications, the air-core coil is usually slow moving and needs to hold at a position during operations. When the air-core coil is stationary, i.e., no work done, it can be assumed that all the power generated from the coil turns into heat. Thus, the elevation and saturation of coil temperature will reflect the thermal characteristic of the EDM, which is crucial for understanding the thermal stability of FELA. Based on the architecture of the cylindrical-shaped FELA, the moving air-core is located in the center while the stator and other structures constitute the thermal paths to dissipate heat to the external environment. The thermal performance can be represented as a classical analogous lumped-element circuit model that comprises of thermal resistors and capacitors [23]. Based on this approach, the thermal resistance of an element, \mathbb{R} , is given as

$$\mathbb{R} = \frac{\mathbb{L}}{A h} \quad (7)$$

where \mathbb{L} represents the length of the thermal path, A represents the cross-sectional area of the thermal path, and h represents the thermal conductivity of the thermal path. In addition, the thermal capacitance of an element, \mathbb{C} , is given as

$$\mathbb{C} = M H_s \quad (8)$$

where M and H_s represent the mass and the specific heat capacity of the element respectively. By differentiating the transient behavior of a resistance–capacitance (RC) circuit, the rate of change in temperature is expressed as

$$\Delta T = Q \mathbb{R} \left[1 - \exp\left(-\frac{t}{\tau}\right) \right] \quad (9)$$

where t represents the time and τ represents the thermal time constant, i.e., $\tau = M H_s \mathbb{R}$.

3.3. Thermal model of the EDM

Based on the lumped capacitance modeling approach, the thermal path of the cylindrical-shaped EDM is represented by two cascaded RC circuits as shown in Fig. 5. The source of this circuit is the temperature of the air-core coil, which is represented by T_{coil} ,

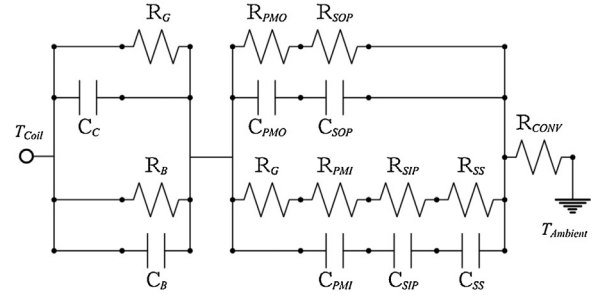


Fig. 5. RC circuit representation of the cylindrical-shaped EDM.

and the ground represents the ambient temperature outside of the EDM, i.e., $T_{Ambient}$. The first RC circuit represents the thermal path of the air gap between the surface of the air-core coil and the surface of the outer PM where \mathbb{R}_G represents the thermal resistance of the air gap while \mathbb{C}_G represents the thermal capacitance of the coil. In addition, it also contains the parallel thermal path of heat transfer from the air-core coil to the bobbin that holds it where \mathbb{R}_B represents the thermal resistance of the air gap while \mathbb{C}_B represents the thermal capacitance of the coil. For the first RC circuit, the thermal resistance and capacitance are expressed as

$$\mathbb{R}_I = (1/\mathbb{R}_G + 1/\mathbb{R}_B)^{-1} \quad (10)$$

$$\mathbb{C}_I = \mathbb{C}_C + \mathbb{C}_B \quad (11)$$

Based on the first RC circuit, the change of temperature, ΔT_1 , due to the power generated by the input current is given as

$$\Delta T_1 = Q \mathbb{R}_I \quad (12)$$

The second RC circuit represents the parallel thermal paths from the outer PM to the environment and from the inner air gap to the environment. From the outer PM to environment, \mathbb{R}_{PMO} and \mathbb{R}_{SOP} represent the thermal resistance of the outer PM and the stator outer casing respectively while \mathbb{C}_{PMO} and \mathbb{C}_{SOP} represent the thermal capacitance of the outer PM and the stator outer casing respectively. From the inner air gap to environment, \mathbb{R}_G , \mathbb{R}_{PMI} , \mathbb{R}_{SIP} , and \mathbb{R}_{SS} represent the thermal resistance of the inner air gap, inner PM, stator inner shaft, and stator side structure respectively. Similarly, \mathbb{C} represents the thermal capacitance of these elements. For the second RC circuit, the thermal resistance and capacitance are expressed as

$$\mathbb{R}_{II} = [1/(\mathbb{R}_{PMO} + \mathbb{R}_{SOP}) + 1/(\mathbb{R}_G + \mathbb{R}_{PMI} + \mathbb{R}_{SIP} + \mathbb{R}_{SS})]^{-1} + \mathbb{R}_{CONV} \quad (13)$$

$$\mathbb{C}_{II} = (1/\mathbb{C}_{PMO} + 1/\mathbb{C}_{SOP})^{-1} + (1/\mathbb{C}_{PMI} + 1/\mathbb{C}_{SIP} + 1/\mathbb{C}_{SS})^{-1} \quad (14)$$

Based on the second RC circuit, the change of temperature, ΔT_2 , due to the power generated by the input current is given as

$$\Delta T_2 = Q \mathbb{R}_{II} \quad (15)$$

A generic temperature–time characteristic of the air-core coil due to a constant current input over a period of time is plotted in Fig. 6. ΔT_1 , which is contributed by the first RC circuit, occurs rapidly because the thermal path is short due to the small air gap between the coil and the PM. In addition, the rise is linear as the thermal capacitance of the bobbin is low due to its small volume mass that is unable to store much heat. Hence, the heat generated from the coil is quickly dissipated to the surrounding PMs. In most cases, ΔT_1 would be at 95% of its final value by 3τ . On the other hand, the temperature rise from ΔT_1 to ΔT_2 is usually longer and nonlinear as compared to ΔT_1 . This is because there are more elements in the second RC circuit that lead to higher thermal resistance

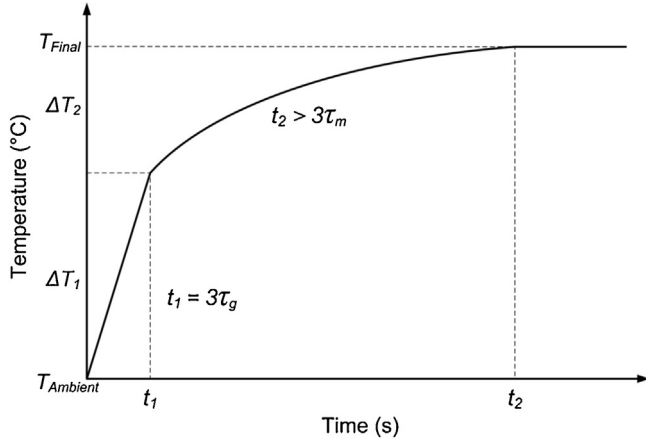


Fig. 6. A generic temperature-time graph of an air-core coil when introduced with a constant current over a period of time.

Table 1

Selected values for the thermal properties of different elements.

Elements	Thermal properties	Values
Copper (Coil wire)	Density (kg/m ³)	8940
	Specific heat capacity (J/kg K)	390
	Thermal conductivity (W/m K)	400
Iron (Stator)	Density (kg/m ³)	7850
	Specific heat capacity (J/kg K)	449
	Thermal conductivity (W/m K)	80
Rare-earth (PMs)	Density (kg/m ³)	7400
	Specific heat capacity (J/Kg K)	506
	Thermal conductivity (W/m K)	17
Aluminum (Non-ferrous parts)	Density (kg/m ³)	2700
	Specific heat capacity (J/Kg K)	900
	Thermal conductivity (W/m K)	250

and capacitance. Higher thermal resistance will cause the temperature rise to be slow and higher thermal capacitance will cause nonlinearity. In most cases, it will take more than 3τ before ΔT_2 reaches 95% of its final value. Without considering the transient temperature over a period of time, the final saturation temperature of the air-core coil is expressed as

$$T_{final} = T_{Ambient} + \Delta T_1 + \Delta T_2 \quad (16)$$

Lastly, Table 1 lists the selected values for the thermal properties of different elements that are used to calculate the saturation temperature of the air-core coil based on the thermal resistance and capacitance of the proposed RC circuit.

4. Stiffness modeling of the flexure-based membrane support bearings

After designing the cylindrical-shaped EDM based on the presented thermal modeling, the predicted output force at the desired operating temperature will be used to design the flexure-based membranes. Fig. 7 illustrates a flexure-based membrane support articulated by four parallel beam-based flexure joints. The length of each beam-based flexure joint is a combination of four folds of flexible beams, which are coupled together to deliver a pure translational motion. With the fixed segment attached to the stator of the EDM, a single-DOF motion is produced at the moving segment through the deflection of these beam-based flexure joints.

4.1. Semi-analytic model

The stiffness of the flexure-based membrane can be obtained using the semi-analytic model [19]. This theoretical model provides

a simple and generic solution for approximating the large non-linear deflection of any beam-based flexure configuration, i.e., a beam-based flexure coupled with a rigid-link of any length, shown in Fig. 7d. The accuracy and robustness of the proposed model is ensured by considering two crucial factors while adopting the principle of using a torsional spring to represent the stiffness of a beam-based flexure joint. The first factor is the parasitic shifting of the 'pivot' joint of a beam-based flexure joint during large deflection, while the second factor is the changing angular stiffness of the torsional spring. With all derivations being presented in previous work [19], the semi-analytic model states that the deflection of a flexure configuration is given as

$$\delta = \left(L + \frac{l}{2\varpi} \right) \sin \alpha \quad (17)$$

where α represents the deflection angle and ϖ is a Sinc function, i.e., $\varpi = \sin \alpha / \alpha$. The resultant parasitic motion, δ_p , normal to the deflection axis is given as

$$\delta_p = \left(L + \frac{l}{2} \right) - \left(L + \frac{l}{2\varpi} \right) \cos \alpha \quad (18)$$

The loading force, F , is expressed as

$$F = \frac{E I \alpha}{l(L + (\rho l / 2\varpi)) \sin((\pi/2) - \alpha)} \quad (19)$$

where E and I represent the Young's Modulus and second moment of area of the flexure joint respectively, while ρ is

$$\rho = \frac{l\sqrt{1.8} + L}{l + L} \quad (20)$$

The maximum bending stress, σ_{max} , is given as

$$\sigma_{max} = \frac{F[l/2 + (L + l/2\varpi) \cos \alpha](h/2)}{I} \quad (21)$$

where h represents the thickness of the flexure joint.

(Note: Termed as semi-analytic model since deflection or loading force can be solved directly with a given deflection angle while solving deflection angle based on a known deflection or loading force would require iterative root-finding procedures, e.g., Newton-Raphson method, etc.)

4.2. Modeling of the flexure-based membrane

In this work, the flexure-based membranes are made up of beam-based flexure joints with no rigid-link coupled to them. Hence, $L=0$ when using the semi-analytic model. The deflection stiffness along the x -axis of a beam-based flexure joint with no rigid-link is denote as K_δ . Hence, the loading of the beam-based flexure joint becomes a point force. However, the point force loading does not permit a pure translational motion. As each flexure membrane is a supporting bearing for the air-core coil translating in a single linear motion, the beam-based flexure joint must be modeled as a cantilever beam with a pure translation motion. To deliver a pure translation motion, each beam-based flexure joint deflects in "S"-like shape and can be represented as two identical beam-joints with individual length being $l/2$ and the desired translation motion, Δ , becomes twice of the deflection of each beam-joint, i.e., $\Delta/2$, as shown in Fig. 7c. Hence, the translation stiffness is given as

$$K_j = 2 \frac{F_\Delta}{\Delta} \quad (22)$$

where driving force, F_Δ , is obtained from Eq. (19) using the deflection angle, α , derived from Eq. (17) based on $\delta = \Delta/2$, $l \rightarrow l/2$, and $L=0$. With each limb being formed by two identical beam-joints connected in series, the translation stiffness along the x -axis of each limb, K_L , is half of a beam-joint, i.e., $K_L = K_j/2$. Consequently,

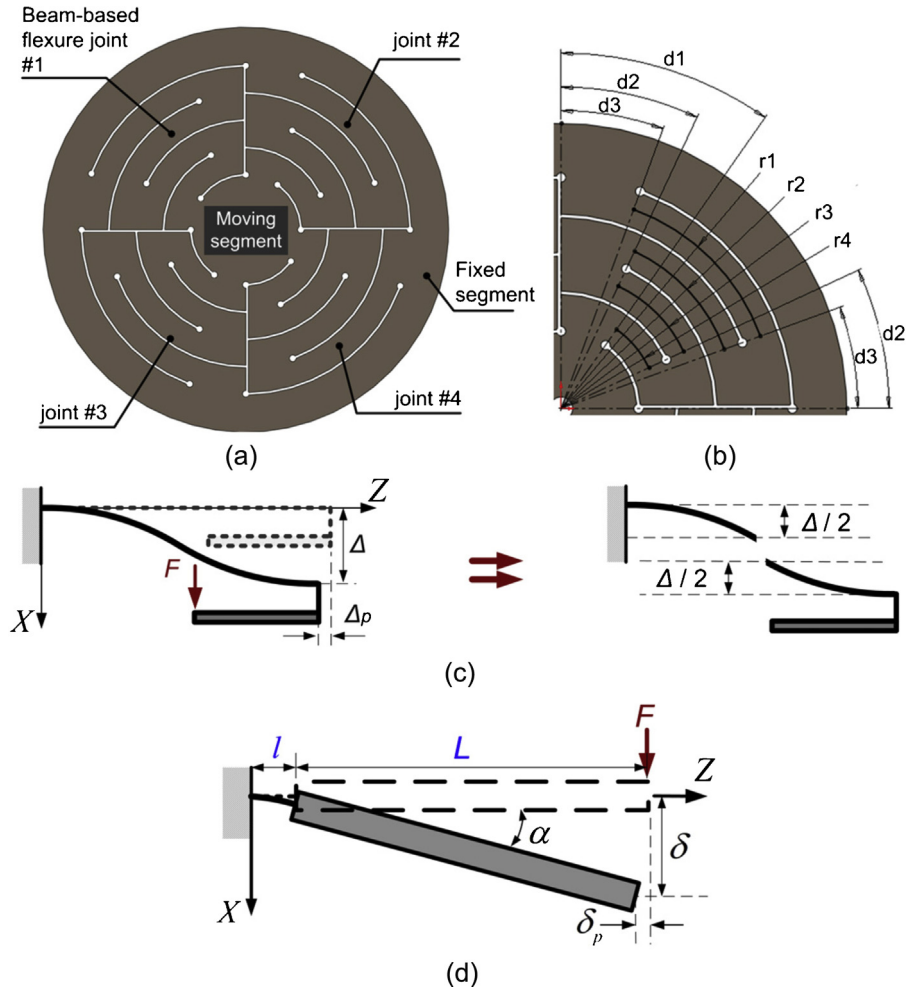


Fig. 7. (a) A flexure-based membrane support bearing articulated by four parallel beam-based flexure joints. (b) Each beam-based flexure joint combines four folds of flexible beams to deliver (c) a pure translational motion. (d) Illustration of a generic beam-based flexure configuration.

the translation stiffness of a pair of flexure-based membrane is governed by

$$K_{\delta} = 8K_L \quad (23)$$

As mentioned, the length of each beam-based flexure joint is a combination of four folds of flexible beams. The length of each flexible beam is represented as

$$l_j = (90^\circ - d) \left(\frac{\pi}{180^\circ} \right) r \quad (24)$$

where j represents the beam number $\{i = 1, 2, 3, 4\}$, d is the angle (in degree) and r is the radius of each arc that represents the length of the beam as shown in Fig. 7b. From the fixed segment to the moving segment, $d = 2(d_3)$ and $r = r_1$ to determine the length of flexible beam #1, $d = d_2 + d_3$ and $r = r_2$ to determine the length of flexible beam #2, $d = 2(d_2)$ and $r = r_3$ to determine the length of flexible beam #3 and $d = d_1 + d_2$ and $r = r_4$ to determine the length of flexible beam #4. Subsequently, the length of each beam-based flexure joint is given as

$$l = \sum_{j=1}^4 l_j \quad (25)$$

5. Prototype

The presented analytical models were used to synthesize the cylindrical-shaped FELA based on the targeted specifications, i.e., ± 20 nm positioning stability and $\pm 0.15^\circ\text{C}$ thermal stability over a stroke length of 2 mm at the end-effector. In addition, the overall dimension must not exceed $\varnothing 50 \times 100 \text{ mm}^2$ due to size constraint of the entire positioning system. Based on the magnetic field model derived in [22,18], the thickness of the PMs within the segmented DM configuration were selected as 6 mm with a length of 50 mm. Using the presented thermal model, the cylindrical-shaped EDM was predicted to produce a constant current-force sensitivity of 10.15 N/A. To achieve a thermal stability of $\pm 0.15^\circ\text{C}$, the stiffness of a pair of supporting flexure-based membranes plays a crucial role as the EDM must operate near ambient temperature, i.e., 20°C . Using the presented model to synthesize the pair of flexure-based membrane support bearings, the bearings were eventually designed with a predicted stiffness of 1375 N/m. As a result, only 0.136 A is required to generate 1.38 N to achieve ± 1 mm. Based on the thermal model, the temperature of the air-core coil within the cylindrical-shaped EDM will rise by 0.7°C after 1.5 h. As this predicted performance can satisfy the targeted specifications, a cylindrical-shaped FELA prototype based on the synthesized EDM and flexure-based membranes was developed as shown in Fig. 8. Table 2 lists the parameters and actual specifications of the

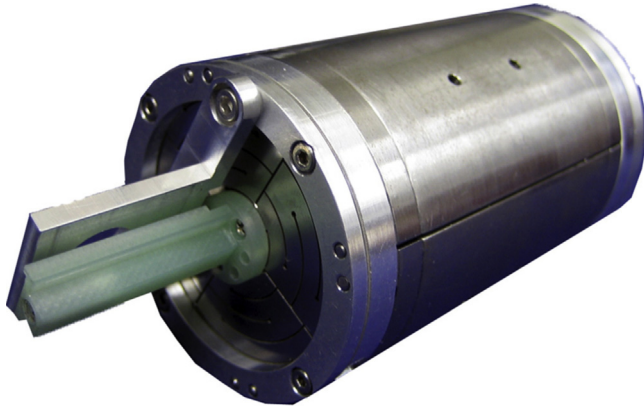


Fig. 8. Prototype of the new cylindrical-shaped FELA.

Table 2

Parameters and specifications of the cylindrical-shaped EDM and the flexure-based membrane support bearing.

	Specifications
<i>Cylindrical-shaped EDM</i>	
Wire diameter, OD	0.48 mm (insulation layer ~ 0.03 mm)
Coil resistance, R_{coil}	5.93 Ω
<i>Flexure-based membrane</i>	
Material	SUS301 Full-hard
Young's modulus	193 GPa
Thickness	0.2 mm
Width	3 mm
Angle of arc, d	$d1 = 35^\circ$, $d2 = 25^\circ$, $d3 = 20^\circ$
Radius of arc, r	$r1 = 18.20$ mm, $r2 = 14.90$ mm, $r3 = 11.60$ mm, $r4 = 8.30$ mm

cylindrical-shaped EDM and the flexure-based membrane support bearing.

6. Experiments and results

6.1. Thermal characteristic of the cylindrical-shaped EDM

An experiment was conducted to investigate the thermal characteristic of the cylindrical-shaped EDM and to evaluate the accuracy of the proposed model. A thermocouple sensor (RT-100) was attached onto the surface of the air-core coil and connected to a computer to log the temperature at an interval of 1 s. Temperature measurement was taken only with the cylindrical-shaped EDM because the thermal characteristic was modeled without the flexure-based membranes and supporting components. To prevent heat loss through any material that is not part of the prototype, it was placed on a carbon fiber composite board, which was treated as an isolator. A set of constant current inputs was used to energize the air-core coil and temperature of the coil was logged until it saturated, i.e., about 1.5 h after being energized. The predicted and measured coil temperature based on the constant current values are listed in Table 3. A comparison between the predicted and measured temperature values shows that the presented analytical model is accurate in predicting the coil temperature with a

Table 3

Predicted and measured coil temperature after 1.5 h based on constant input current.

Current (A)	Power (W)	Coil temperature after 1.5 h ($^{\circ}$ C)	
		Predicted	Measured
0.1	0.059	20.4	20.3
0.4	0.949	26.2	28.0
0.5	1.483	29.6	32.0

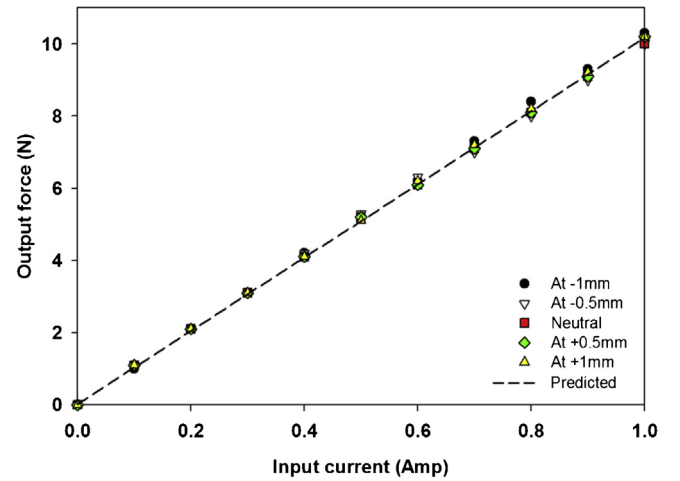


Fig. 9. Current-force relationship of the cylindrical-shaped EDM due to different positions of the air-core coil translator.

maximum deviation of 7.5% obtained the investigation. The slight deviation is contributed by variation in the internal coil resistance where actual value is measured at 5.93 Ω while the predicted value is 5.31 Ω . In addition, the selected values for each thermal property listed in Table 1 may differ from the actual values. Nevertheless, the experimental results have shown that the developed cylindrical-shaped EDM has achieved the desired thermal characteristic.

6.2. Current-force sensitivity of the cylindrical-shaped EDM

To evaluate the current-force sensitivity, the FELA prototype was mounted on a linear guide that locked the cylindrical-shaped EDM at any position along the displacement range. A force sensor (ATI, Nano40) was attached to the output shaft with the other end of the sensor mounted on a fixed wall. The flexure-based bearings ensure that no friction force will be contributing the force measurement. When the air-core coil was energized by an amount of current, the output shaft moved against the force sensor, which picked up the amount of force generated. The linear guide with a locking mechanism allows the cylindrical-shaped EDM to change its position with respect to the fixed air-core coil. As a result, the current-force sensitivity at different positions can be evaluated.

The selected positions along the displacement range to evaluate the current-force sensitivity were neutral position, ± 0.5 and ± 1 mm. At each position, a power supply source was used to energize the air-core coil from 0 to 1 A with an interval of 0.1 A. Fig. 9 plots the input current and output force when the air-core coil was at all selected positions w.r.t. the fixed EDM. It shows that the relationship between input current and output force obtained from all five positions are very consistent and the deviations between the experimental and predicted results are less than 8.35%. Table 4 summarizes the current-force sensitivity at all selected positions. Results show that the current-force sensitivity at various positions along the displacement range are consistent with a deviation of 0.58% recorded between the maximum and minimum values. Subsequently, the average current-force sensitivity throughout the entire stroke measured from the developed prototype is 10.3 N/A. The achieved current-force sensitivity is close to the predicted value of 10.2 N/A. Most importantly, this investigation shows that

Table 4

Current-force sensitivity at various positions along the traveling range.

Pos (mm)	-1.0	-0.5	Neutral	+0.5	+1.0
Current-force (N/A)	10.36	10.34	10.30	10.32	10.36

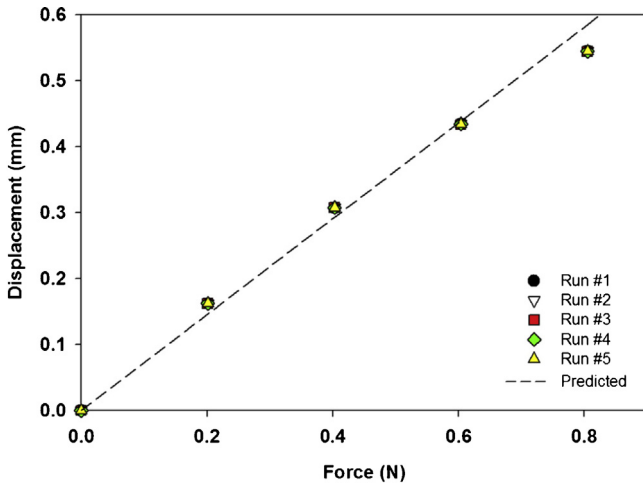


Fig. 10. Experimental results and theoretical prediction on the stiffness of a pair of flexure-based membranes.

the developed cylindrical-shaped FELA has achieved a near constant current–force sensitivity throughout 2 mm stroke.

6.3. Stiffness of the flexure-based membrane support bearing

Stiffness of the flexure-based membrane support bearing governs the relationship between the force generated from the EDM and the displacement of the output shaft. To evaluate the stiffness of these bearings, a high resolution current source (KEITHLEY 224/2243) was used to energize the EDM and the generated displacement of the output shaft was measured by a high resolution optical linear encoder (MicroE Systems, M3500). In this work, high resolution current source was used because it provides very stable current output. Hence, very stable step displacements can be obtained to reduce measurement errors. Subsequently, the force generated due to the input current was determined based on the current–force sensitivity of 10.3 N/A. With the measured displacement and predicted force, the actual stiffness of the pair of flexure-based membrane support bearings was obtained and plotted in Fig. 10. The predicted stiffness of 1375 N/m obtained from the semi-analytic model was also plotted against the measured values. Results show that the pair of flexure-based membrane support bearings has an average stiffness of ≈ 1398 N/m. Although the input current was restricted to 80 mA due to the limitation of the current source, the trend suggests that the stiffness of the flexure-based membrane support bearings is linear throughout the targeted stroke range. Most importantly, this investigation shows that the semi-analytic model is accurate in predicting the stiffness with a maximum deviation of 7.15%.

6.4. Reconfiguring the open-loop positioning resolution

This section presents how the open-loop positioning resolution of FELA can be reconfigured by changing the thickness of the flexure-based bearings or by adding an external resistor.

6.4.1. Changing the thickness of the flexure-based bearings

Governed by Eq. (3), a change in the stiffness of the flexure-based bearing will alter the open-loop positioning resolution. In Eq. (19), the second moment of area is expressed as

$$I = \frac{bt^3}{12} \quad (26)$$

where b and t represent the width and the thickness of the flexure respectively. Based on Eq. (26), changing the thickness is the most

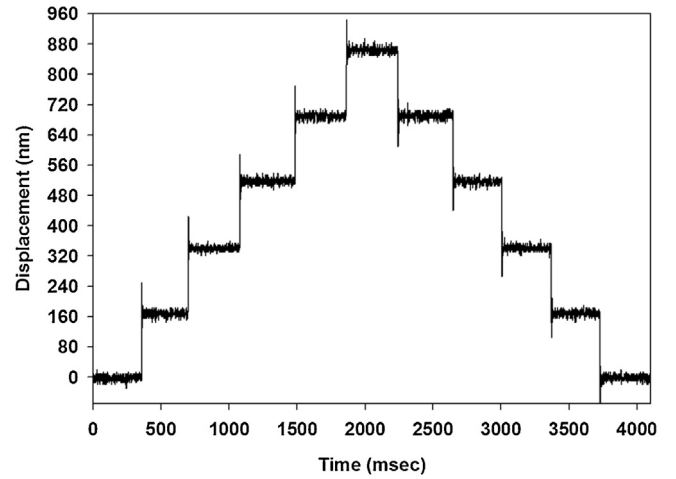


Fig. 11. Open-loop step displacements of FELA using flexure-based bearing with 0.2 mm thickness.

effectively approach in altering the stiffness of the flexure-based bearing. In this work, an investigation, which involved the FELA prototype, was conducted to demonstrate such flexibility. Based on the initial thickness of 0.2 mm, a set of input current, i.e., from $i = 22$ to $110 \mu\text{A}$ at an interval of $22 \mu\text{A}$, via the high resolution current source, was used to energize the moving air-core coil so as to step the output shaft forward and return to neutral position. The step displacements of the output shaft were recorded by the high resolution optical encoder (5 nm/count) and plotted in Fig. 11. At $22 \mu\text{A}$, a displacement of 172 nm was achieved and 345 nm was achieved at $44 \mu\text{A}$. Hence, the open-loop positioning sensitivity was $7.82 \text{ nm}/\mu\text{A}$.

Next, the thickness of each flexure-based bearing was changed from 0.2 to 0.5 mm at an interval of 0.1 mm. For each thickness change, similar set of input current was used to drive the output shaft forward and return to neutral position. Based on a pair of flexure-based bearings with 0.3 mm thickness, the semi-analytic model predicted a stiffness of 4641 N/m. For 0.4 mm thickness, the predicted stiffness for the bearings is 11003 N/m. For 0.5 mm thickness, the predicted stiffness is 21485 N/m. Using the measured current–force sensitivity, i.e., 10.3 N/A, the step displacements of FELA were predicted and listed in Table 5 based on different bearing thickness and input current values. The experimental results

Table 5

Reconfiguring the open-loop step displacement of FELA using flexure-based bearings with different thickness.

Current (μA)	Predicted	Measured (avg)	Error (%)
<i>0.3 mm thickness: Step displacement (nm)</i>			
22	45.43	42.69	6.42
44	89.46	86.00	4.02
66	133.83	130.69	2.41
88	177.16	174.37	1.60
110	221.18	212.43	4.12
<i>0.4 mm thickness: Step displacement (nm)</i>			
22	19.15	20.56	6.84
44	37.59	37.66	0.17
66	56.17	54.36	3.32
88	74.74	74.98	0.31
110	93.17	94.89	1.82
<i>0.5 mm thickness: Step displacement (nm)</i>			
22	9.88	10.00	1.17
44	19.48	20.00	2.62
66	28.92	30.00	3.61
88	38.42	40.00	3.95
110	47.86	50.00	4.28

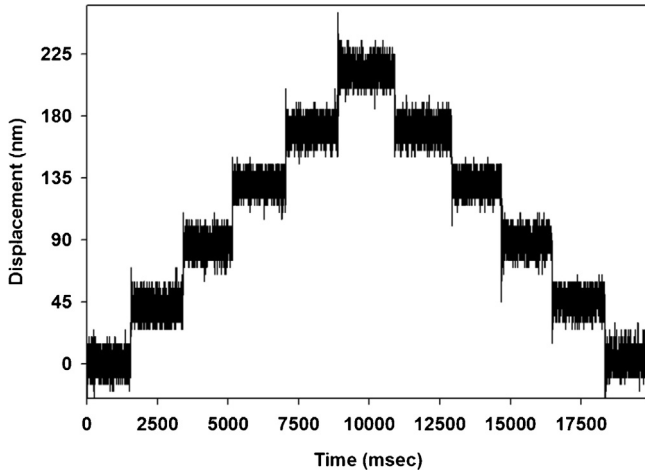


Fig. 12. Open-loop step displacements of FELA supported by flexure-based bearings with 0.3 mm thickness.

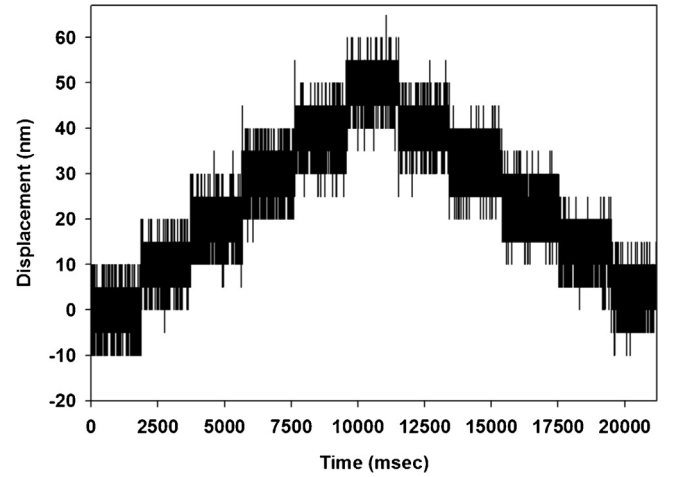


Fig. 14. Open-loop step displacements of FELA supported by flexure-based bearings with 0.5 mm thickness.

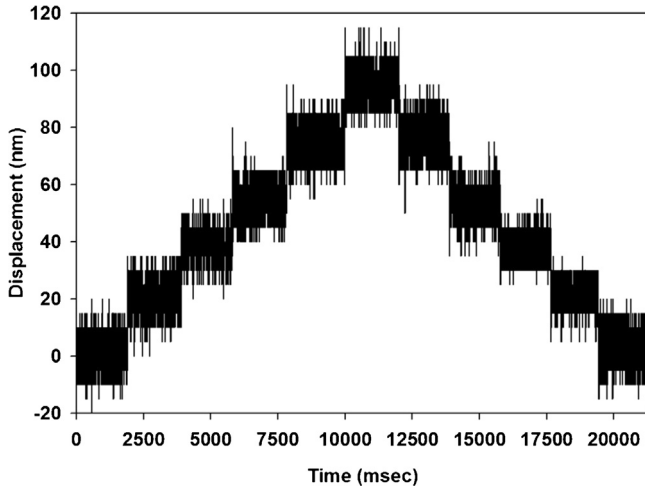


Fig. 13. Open-loop step displacements of FELA supported by flexure-based bearings with 0.4 mm thickness.

show that the measured step displacements agree with the predicted values. With a maximum deviation of 6.84% found between the measured and predicted values, this experimental investigation shows that the semi-analytic model is accurate in predicting the stiffness for such kind of flexure joint configuration, i.e., $L=0$. Most importantly, results also show that the open-loop positioning resolution of FELA is predictable.

Figs. 12–14 plot the actual step displacements of FELA supported by flexure-based bearings with thickness of 0.3, 0.4, and 0.5 mm respectively. Referring to Fig. 12, the open-loop positioning sensitivity of FELA was enhanced from 7.82 to 1.94 nm/ μ A when the thickness of the flexure-based bearings changed from 0.2 to 0.3 mm. With thickness of 0.4 mm, the open-loop positioning sensitivity was further improved to 0.93 nm/ μ A. Lastly, FELA produced an open-loop positioning sensitivity of 0.45 nm/ μ A with the flexure-based bearings having a thickness of 0.5 mm. Experimental results show that the open-loop positioning resolution of FELA is reconfigurable by changing the thickness of the flexure-based bearings.

On the other hand, the achievable displacements were also affected by such changes. By comparing the final displacements plotted in both Fig. 12 and 14, a FELA, which was supported by flexure-based bearings with thickness of 0.3 mm, achieved 212.43 nm at 110 μ A. With the same amount of input current,

the FELA, which was supported by flexure-based bearings with thickness of 0.5 mm, achieved just 50 nm. This comparison suggests that although the open-loop positioning sensitivity of FELA can be enhanced by increasing the thickness of the flexure-based bearings, this approach requires more force to overcome the increasing stiffness of those bearings. Consequently, more heat will be generated due to the increase of input current. In addition, changing the stiffness has a direct effect on the dynamics of the FELA. Assuming the moving mass remains unchanged, reducing the stiffness so as to minimize heat generation will reduce the dynamic performance, i.e., natural resonant frequency. On the other hand, both dynamic behavior and open-loop positioning resolution can be enhanced by increasing the stiffness of the flexure-based bearings. Most importantly, the results obtained from the experimental investigation have demonstrated that the open-loop positioning resolution of FELA is predictable and reconfigurable by changing the thickness of the flexure-based support bearings.

6.4.2. Adding an external resistor

An alternate approach to enhance the open-loop positioning resolution of FELA without affecting the heat generation is by making use the Ohm's Law. From Eq. (3), adding an external resistor, R_{ext} in series with FELA will reduce the amount of current energizing the EDM via the voltage mode. Consequently, less amount of current will lead to less force generation and thus produce smaller step displacement. An experimental investigation was conducted to demonstrate how external resistance loads can enhance the open-loop positioning resolution.

At initial conditions, i.e., flexure-based bearings with 0.2 mm thickness, internal coil resistance, $R_{coil} = 5.93 \Omega$, and $R_{ext} = 0 \Omega$, a set of input voltage, i.e., from VDC = 0.064 to 0.256 mV at an interval of 0.064 mV was used to drive the output shaft forward and return to neutral position. The step displacements of the output shaft were recorded by the same optical encoder as plotted in Fig. 15. At 0.064 mV, a step displacement of 172.87 nm was achieved by the FELA. At 0.256 mV, a step displacement of 345 nm was produced. Hence, the open-loop positioning sensitivity was 1347.66 nm/mV. Next, R_{ext} was increased to 5, 15, and 25 Ω respectively. For every increment, the same set of input voltage was used to drive the output shaft while the optical encoder recorded the step displacements. Table 6 lists the measured step displacements of FELA due to different external resistance loads.

Using Eq. (3), the current–force sensitivity of 10.3 N/A, $R_{coil} = 5.93 \Omega$ and stiffness of 1375 N/m, the predicted step

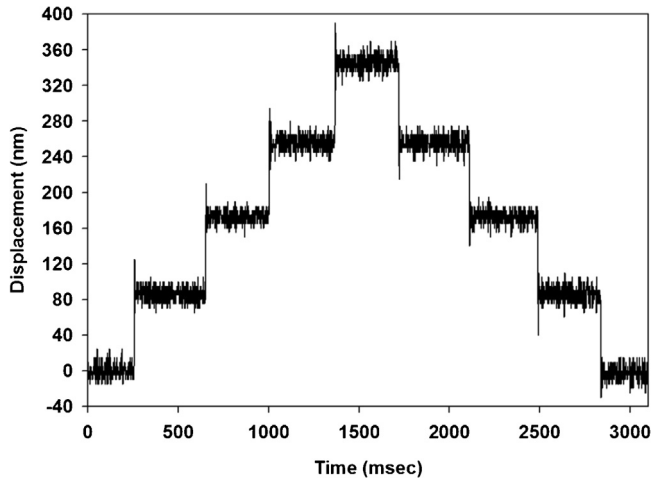


Fig. 15. Open-loop step displacements of FELA at initial conditions.

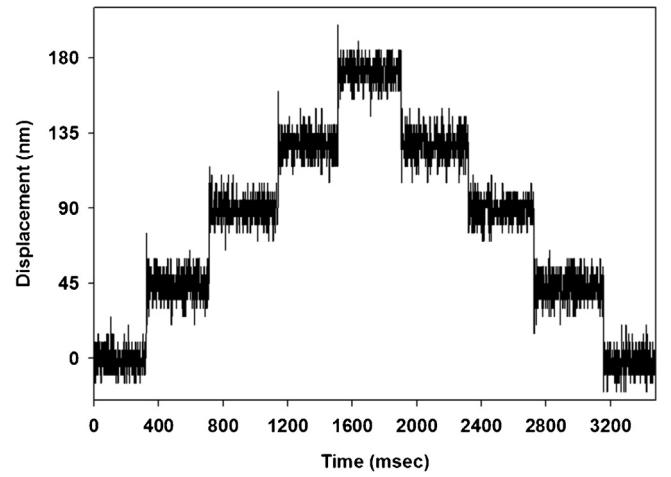


Fig. 16. Open-loop step displacements of FELA when $R_{ext} = 5 \Omega$.

Table 6

Reconfiguring the open-loop step displacement of FELA by adding different external variable resistance.

Voltage (mV)	Predicted	Measured (avg)	Error (%)
<i>$R_{ext} = 5 \Omega$: Step displacement (nm)</i>			
0.064	43.43	43.02	0.95
0.128	88.37	89.23	0.98
0.192	125.81	128.84	2.41
0.256	168.50	171.99	2.08
<i>$R_{ext} = 15 \Omega$: Step displacement (nm)</i>			
0.064	23.22	25.11	8.17
0.128	45.68	46.78	2.42
0.191	68.90	70.94	2.96
0.256	92.11	95.52	3.70
<i>$R_{ext} = 25 \Omega$: Step displacement (nm)</i>			
0.064	15.73	15.52	1.29
0.128	30.70	28.46	7.32
0.192	46.80	44.77	4.36
0.256	62.53	61.43	1.77

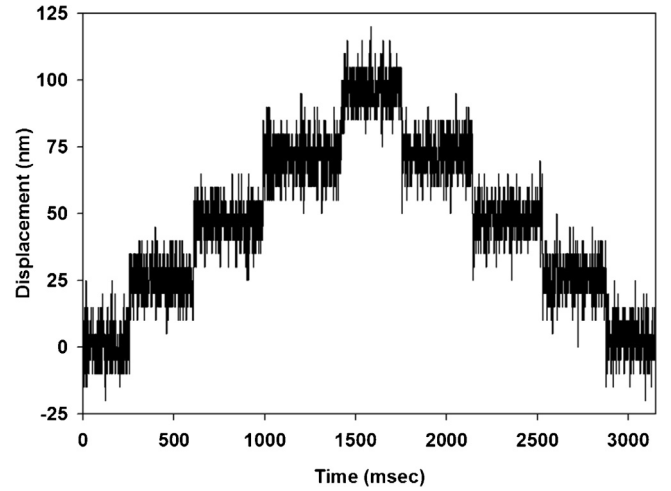


Fig. 17. Open-loop step displacements of FELA when $R_{ext} = 15 \Omega$.

displacements of FELA at different external resistance loads are also listed in Table 6. For every change of external resistance load, the experimental results show that the step displacements of FELA were well predicted by Eq. (3). The measured step displacements agree with the predicted values and the maximum deviation between them is 8.17%. Using the same set of input voltage, the experiment also show that the step displacements of FELA reduced when the external resistance load increased. Results have proven that the assumption of increasing resistance load to lower the input current, which in turn reduce the step displacement, is valid. When $R_{ext} = 5 \Omega$, the measured open-loop positioning sensitivity became 362.81 nm/mV. When $R_{ext} = 25 \Omega$, the measured open-loop positioning sensitivity became 245.78 nm/mV. Results show that the open-loop positioning sensitivity of FELA was increased from the initial 1347.66 to 245.78 nm/mV just by adding a 25 Ω external resistor. Consequently, this experimental investigation has demonstrated that the open-loop positioning resolution is predictable and reconfigurable through an external resistance load.

As compared to changing the thickness of the flexure-based bearings, there are two main advantages of using an external resistance load to configure the open-loop positioning resolution. First, this approach will not increase the force required to achieve the targeted displacement since the stiffness of the bearings remains unchanged. As a result, targeted displacement can still be achieved without increasing the input current. Thus, the thermal characteristics of the FELA remains unchanged. Second, the flexibility

is higher as compared to changing the thickness of the bearings. In real applications, adding an external resistance load in series with FELA is more flexible than changing the thickness of the support bearings. In addition, thickness of these stainless steel shims are limited to certain range or specific thickness. The limitation of adding external resistance load is that this approach cannot reduce the noise level caused by the environmental disturbance. Figs. 16–18 plot the actual open-loop step displacements of FELA when $R_{ext} = 5, 15$ and 25Ω respectively. At different external resistance loads, the average positioning noise is always ± 15 nm. From Fig. 12–14, the average positioning noise drops from ± 15 to ± 10 nm due to change in the stiffness of the flexure-based bearings. As a result, Fig. 14 shows more stable open-loop step displacements plot as compared to Fig. 18. Another limitation of adding external resistance load is that the overall power consumption of the system will increase. Although this increase in power consumption has no effect in the heat generation since the external load is outside of FELA, the wattage of the power source, which drives the entire system, needs to be increased accordingly to the added resistance. Although each approach has its limitations, both approaches are able to configure the open-loop positioning resolution of FELA. Choosing between two approaches will depend very much on the targeted applications and a good understanding of the performance trade-offs.

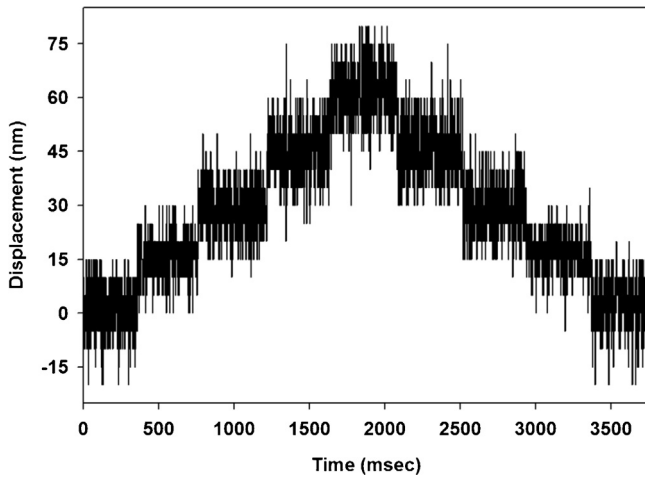


Fig. 18. Open-loop step displacements of FELA when $R_{ext} = 25 \Omega$.

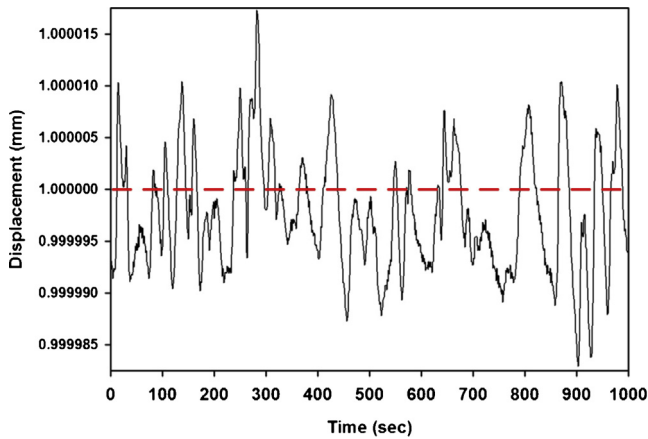


Fig. 19. Positioning stability at 1 mm with PID servo-control.

6.5. Evaluating the positioning and thermal stability

Using the same optical encoder as the position feedback sensor of the output shaft, a Proportional-Integral-Derivative (PID) control was implemented to control the positioning of the FELA. Through the PID control scheme, FELA achieved a closed-loop positioning resolution of ± 10 nm at ± 1 mm. A laser interferometer system (SIOS, resolution: 1 nm/count) was used to evaluate the

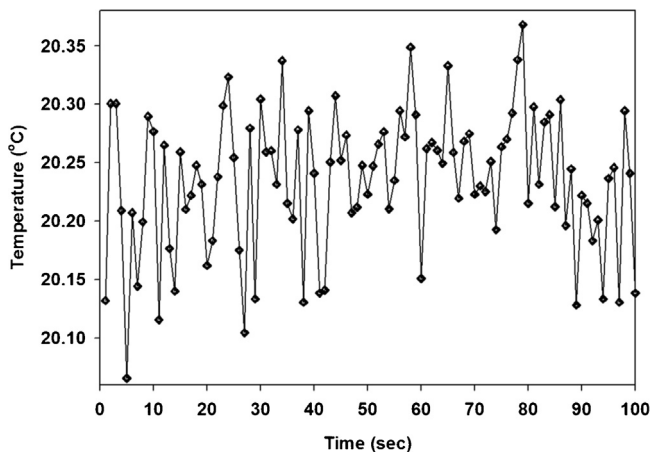


Fig. 20. Operating temperature of coil at 1 mm.

actual positioning accuracy at the tip of the output shaft. At 1 mm, Fig. 19 shows that the tip of the output shaft is capable of delivering an average positioning stability of ± 10 nm. Fig. 20 plots the temperature of the coil when FELA was operating at 1 mm. It shows that the coil temperature remained at 20.25°C with a thermal stability of $\pm 0.15^\circ\text{C}$. Based on the measured flexure-based bearing stiffness of 1398 N/m and current–force sensitivity of 10.3 N/A, the estimated input current is approximately 0.135 A (0.8 W). Based on this amount of input current, the thermal model predicted that the coil temperature will increase to 20.4°C by approximately 92 s (1.5 min). The predicted temperature and time almost agree with the coil temperature profile plotted in Fig. 20 with a deviation of 0.15°C .

7. Conclusion

This paper has presented a novel nanopositioning actuator that achieves a large stroke range of ± 1 mm with a positioning stability of ± 10 nm and a thermal stability of $\pm 0.15^\circ\text{C}$. To achieve such desired thermal characteristics, a thermal model of the Lorentz-force EDM based on lumped capacitance modeling approach was presented. Experimental investigations have shown that the presented thermal model is accurate in predicting the coil temperature. This paper also presented a novel semi-analytic modeling approach that was used to synthesize the proposed flexure-based membrane support bearings. Experimental evaluations have shown that the proposed semi-analytic model is accurate in predicting the stiffness of such bearings. The unique characteristics of the nanopositioning actuator, i.e., predictable and re-configurable open-loop positioning resolution, were also demonstrated. Two approaches were presented on how to re-configure the open-loop positioning resolution. Advantages and disadvantages of each approach were discussed in detail. With the FELA, the future work will focus on the implementation of this actuator on applications such as stem-cell manipulation and fiber optics alignment.

References

- [1] Kenji U. Piezoelectric actuator and ultrasonic motors. USA: Kluwer Academic Publishers; 1997.
- [2] Pham H-H, Chen I-M. Stiffness modeling of flexure parallel mechanism. *Precis Eng* 2005;29(4):467–78.
- [3] Sok CW, Youcef TK. Modeling of an omni-directional high precision friction drive positioning stage. In: IEEE international conference on robotics and automation. 1998. p. 175–80.
- [4] Lia J, Sedaghatia R, Dargahia J, Waechterb D. Design and development of a new piezoelectric linear inchworm actuator. *Mechatronics* 2005;15: 651–81.
- [5] Yamagata Y, Higuchi T. A micropositioning device for precision automatic assembly using impact force of piezoelectric elements. In: IEEE international conference on robotics and automation. 1995. p. 666–71.
- [6] Sprenger B, Binzel O, Siegwart R. Control of a high performance 3 dof linear direct drive operating with submicron precision. In: 4th international conference on motion and vibration control. 1998. p. 1145–50.
- [7] Lum GZ, Teo TJ, Yang G, Yeo SH, Sitti M. Integrating mechanism synthesis and topological optimization technique for stiffness-oriented design of a three degrees-of-freedom flexure-based parallel mechanism. *Precis Eng* 2015;39:125–33.
- [8] Hiemstra DB, Parmar G, Awtar S. Performance tradeoffs posed by moving magnet actuators in flexure-based nanopositioning. *ASME/IEEE Trans Mechatron* 2014;19:1–12.
- [9] Chen KS, Trumper DL, Smith ST. Design and control for an electromagnetically driven x–y–θ stage. *Precis Eng* 2002;26:355–69.
- [10] Mittal S, Meng C-H. Hysteresis compensation in electromagnetic actuators through preisach model inversion. *IEEE Trans Mechatron* 2000;5:394–409.
- [11] Teo TJ, Chen I-M, Yang G, Lin W. A flexure-based electromagnetic linear actuator. *Nanotechnology* 2008;19:315501.
- [12] Teo TJ, Chen IM, Yang G, Lin W. A novel actuator for high-precision alignment in a nano-imprint multi-layers-interconnection fabrication. In: 2007 IEEE international conference on robotics and automation. 2007.
- [13] Kiew CM, Lin WJ, Teo TJ, Tan JL, Lin W, Yang G. Finite element analysis of pmma pattern formation during hot embossing process. In: IEEE/ASME international conference on advanced intelligent mechatronics. 2009. p. 314–9.

- [14] Teo TJ, Kiew CM, Chen I-M, Yang G, Lin W. Model-based control of a high precision imprinting actuator for micro-channel fabrications. In: 2010 IEEE international conference on robotics and automation. 2010. p. 3159–64.
- [15] Teo TJ, Yang G, Chen I-M. A large deflection and high payload flexure-based parallel manipulator for UV nanoimprint lithography: Part I. Modeling and analyses. *Precis Eng* 2014;38(4):861–71.
- [16] Teo TJ, Chen I-M, Yang G. A large deflection and high payload flexure-based parallel manipulator for uv nanoimprint lithography: Part II. Stiffness modeling and performance evaluation. *Precis Eng* 2014;38(4):872–84.
- [17] Hey J, Kiew CM, Yang G, Martinez-Botas R. Model-based compensation of thermal disturbance in a precision linear electromagnetic actuator. *IEEE Trans Mechatron* 2014;19:1477–88.
- [18] Hey J, Teo TJ, Bui VP, Yang G, Martinez-Botas R. Electromagnetic actuator design analysis using a two stage optimization method with coarse-fine model output space mapping. *IEEE Trans Ind Electron* 2014;61:5453–64.
- [19] Teo TJ, Chen I-M, Yang G, Lin W. A generic approximation model for analyzing large nonlinear deflection of beam-based flexure joints. *Precis Eng* 2010;34(3):607–18.
- [20] BEI Kimco Magnetics linear voice coil actuators, online: BEI Kimco Magnetics website (February 2014).
- [21] H2W Technologies voice coil linear actuators, online: H2W Technologies website (February 2014).
- [22] Teo TJ, Chen I-M, Yang G, Lin W. Magnetic field modeling of a dual-magnet configuration. *J Appl Phys* 2007;102(7):074924.
- [23] Button BJ. Heat dissipation and power compression in loudspeakers. *J Audio Eng Soc* 1992;40:32–41.